THE ASTROPHYSICAL JOURNAL, 348:530–541, 1990 January 10

CO LINE FORMATION IN BIPOLAR FLOWS. II. DECELERATED OUTFLOW CASE AND SUMMARY OF RESULTS

SYLVIE CABRIT AND CLAUDE BERTOUT
Institut d'Astrophysique de Paris
Received 1989 March 3; accepted 1989 July 5

ABSTRACT

Following our previous study of accelerated and constant velocity fields, we now investigate CO line formation in decelerated bipolar flows. Position-velocity diagrams and integrated intensity maps are presented for four spatial configurations. These results are used together with previous computations to put constraints on the velocity field and the large-scale structure of observed flows. We suggest that observations might be best explained by a model involving filled CO lobes with a bright, accelerated, high-velocity core surrounded by a slower, low-emissivity envelope. Computed line profiles are also used to estimate the accuracy of various procedures used for deriving the flow parameters from CO data. We find that the most accurate method allows us to estimate the flow force within a factor of ~ 20 and the flow mechanical luminosity within a factor of ~ 60. However, different procedures applied to the same set of CO data give flow parameters that may differ by up to three orders of magnitude.

Subject headings: interstellar: molecules — line formation — nebulae: internal motions — stars: pre–main-sequence — stars: winds

I. INTRODUCTION

The presence of bipolar molecular flows around infrared sources of various luminosities (see Lada 1985 and references therein) shows that young stellar objects often undergo a phase of intense mass loss during which molecular material is anisotropically accelerated to highly supersonic velocities. This energetic phenomenon, unpredicted by theories of star formation, may play a fundamental role in pre–main-sequence evolution by carrying away a large fraction of the angular momentum originally contained in protostellar matter, and by limiting the final mass of the forming star.

Various models of mass ejection and flow collimation from protostellar objects have been proposed to explain the energetics and morphology of bipolar flows (see the reviews of Pudritz 1988 and Boss 1987). CO line observations offer information about the flow structure and velocity field that should allow one to choose between these models. In order to exploit this information, we have developed a code that computes NLTE CO line formation in bipolar outflows with various velocity fields. In the first paper of this series (Cabrit and Bertout 1986, hereafter Paper I), we investigated CO line emission from biconical lobes with accelerated and constant velocity fields and made a first study of uncertainties in the kinematic and dynamic flow parameters derived from CO data. The issue of parameter uncertainties is important because flow energetics give an indirect measure of the mass loss from the underlying protostellar object—averaged over the flow lifetime—and may therefore be used to set constraints on the mechanism driving winds from young stellar objects (e.g., Lada 1985). In Paper I, we found that the simplest procedure used by early observers (from 1980 to about 1983) to derive kinematic and dynamic flow parameters did not give accurate estimates of the model parameters when we applied it to synthetic CO profiles and maps.

In this paper, we extend the analysis of Paper I to decelerated flows and summarize results obtained so far. The computational method is exposed in § II, and synthetic CO maps for an example of decelerated flow are presented in § III. These results are used together with those of Paper I to discuss observational constraints on the structure and velocity field of molecular flows (§ IV). The model that seems best able to reproduce the bulk of CO flow observations involves a bright high-velocity accelerated conical lobe surrounded by a slower low-opacity envelope. Section V summarizes various procedures currently used to derive flow parameters from CO observations and discusses their respective accuracy. We found that the flow mass can now be determined within a factor of 2 and that results obtained using two of these procedures indeed bracket the correct values of flow kinematic and dynamic parameters.

II. METHOD

The flow model is similar to that used in Paper I for accelerated and constant velocity flows, so that line computations for various velocity fields can be directly compared. We consider a high-velocity molecular flow expanding radially in a bicone of opening angle $\theta_{\max}$, inner radius $r_{\min}$, and outer radius $r_{\max} = \sigma r_{\min}$ (see Fig. 1 of Paper I). The velocity field $\boldsymbol{v}(\boldsymbol{r})$ and H_2 density distribution $n_{H_2}(r)$ in the flow are given by

$$\boldsymbol{v}(\boldsymbol{r}) = v_{\max}(r_{\min}/r)^{\alpha}\boldsymbol{u}(\boldsymbol{r}) , \quad \text{where} \quad \boldsymbol{u}(\boldsymbol{r}) = \boldsymbol{r}/r ,$$

and

$$n_{H_2}(r) = n_{H_2}(r_{\min})(r_{\min}/r)^{\delta} .$$

Mass conservation within the flow is assumed, requiring that $\delta = 2 - \alpha$.

a) CO *Excitation*

We assume that CO level populations are in a steady state. Statistical populations of the various rotational levels are then determined from the balance between collisional and radiative transition rates among these levels. The main colliding agent in interstellar molecular clouds is molecular hydrogen, at a kinematic temperature $T_k \sim 10$–20 K. Besides cosmic background

emission at 2.7 K, sources of radiation external to the high-velocity gas are as follows: (1) blackbody radiation from a central star or surrounding warm dust core, (2) thermal emission from dust grains embedded within the flow, and (3) CO line emission from the ambient molecular cloud. These three heating sources are nonetheless negligible, as we now show.

1. The radiation field from a central source of radius r_c and temperature T_c could in principle increase the excitation of surrounding CO molecules by two mechanisms: (*a*) by directly stimulating radiative transitions among rotational levels of the ground state; and (*b*) by populating (through absorption of stellar infrared photons) the first excited vibrational state ($\sim$3000 K above ground level), from which molecules will spontaneously cascade back to excited rotational levels of the ground $v = 0$ state. However, because their effect is roughly proportional to the solid angle filled by the source, both mechanisms are inefficient except at short distances from the central object: less than $\sim r_c(T_c/130\ \mathrm{K})^{1/2}$ for (*a*) and less than about 0.02 pc for (*b*) (Paper I; Carroll and Goldsmith 1981). We can therefore ignore them in our computation of the large-scale high-velocity CO excitation.

2. Assuming dust temperatures $\sim$10 K typical of dark molecular clouds, as well as standard dust absorption law and dust-to-gas ratio (Leung 1975), one can compare the absorption coefficients and emissivities of dust grains to those of CO molecules at the frequencies of the rotational lines of CO. For the range of CO excitation temperatures expected in high-velocity flows, we find that the role of dust can also be neglected (Cabrit and Bertout 1987).

3. CO line photons emitted by the static ambient cloud appear Doppler-shifted in the high-velocity gas rest frame, and can be absorbed only if they propagate at an angle less than $\sin^{-1}(v_{\rm th}/V)$ from the perpendicular to the local flow direction, where V is the outflow velocity and $v_{\rm th}$ the CO thermal line width. Since V ($\geq$10 km s^{-1}) is much larger than $v_{\rm th}$ ($\sim$0.1 km s^{-1} in our model), the corresponding solid angle $\delta\Omega = 4\pi v_{\rm th}/V$ represents a very small fraction of the total solid angle. The contribution of ambient CO line radiation to high-velocity CO excitation is therefore much smaller than that of the cosmic background and is not included in our computations.

We conclude that high-velocity CO gas is heated mainly by cosmic background radiation at $T_b = 2.7$ K and by collisions with H_2 molecules at the local kinetic temperature T_k. Although detection of far-infrared rotational CO emission and of extended vibrational H_2 emission in several molecular flows (e.g., Storey *et al.* 1989; Lane and Bally 1986) suggest the presence of moderate shocks, with postshock temperatures ranging from 200 to 2000 K, we neglect here possible contribution of shock heating to the CO excitation because we are mostly interested in the lowest rotational levels of CO, where emission from preshock gas is expected to dominate (Draine and Roberge 1984) and where excitation temperatures derived from CO (2–1)/(1–0) line ratios are always similar to, or less than, the cloud kinetic temperature (e.g., Snell *et al.* 1984; Levreault 1988).[1] We therefore assume a constant H_2 kinetic temperature throughout the flow, of the order of 10 K.

[1] Excitation of the lowest rotational transitions of CO by slow MHD shocks throughout the flow volume, with shock velocities of the order of the Alfvén velocity ($\sim$1 km s^{-1}; Draine and Roberge 1984), cannot be excluded, since in that case postshock temperatures would be comparable to the cloud kinetic temperature. However, there is at present no observational evidence for such slow shocks, and we chose to ignore them here.

Because the CO thermal width is much smaller than the flow expansion velocity, we adopt the Sobolev approximation to compute CO excitation in the flow (Sobolev 1957). In this limit, the mean radiation intensity can be expressed as the sum of the background intensity and the local value of the source function, weighted by coefficients that depend on the local photon escape probability (see eq. [5] in Paper I). Equations of statistical equilibrium can then be solved independently at each point using an iterative method. The resulting non–LTE level populations at distance r from the star are entirely determined by the values of the following four parameters: the H_2 kinetic temperature T_k, the H_2 number density $n_{\rm H_2}(r)$, the exponent of the velocity law α, and the local Sobolev optical depth $k(r) = (8\pi^3/3h)\mu^2 n_{\rm CO}(r) r/v(r) = k(r_{\rm min})(r_{\rm min}/r)^{(1-2\alpha)}$.

One must be cautious, however, in adopting the local Sobolev approximation for a decelerated flow. When $\alpha > 0$, the radial velocity along a given direction $\boldsymbol{n}$ is not a monotonical function of position as it is for $\alpha < 0$, because the radial velocity gradient along $\boldsymbol{n}$ becomes zero at all positions where $[\boldsymbol{u}(\boldsymbol{r}) \cdot \boldsymbol{n}]^2 = 1/(1+\alpha)$. Hence, at any position $\boldsymbol{r}$ in the flow there exists a particular direction $\boldsymbol{n}$ along which the local radial velocity gradient is zero and the Sobolev approximation does not rigorously hold. This singularity can however be safely ignored in the computation of the mean escape probability without causing major errors in the source function (Bertout 1977). A more profound implication is that two distinct regions of the flow may now have the same radial velocity along $\boldsymbol{n}$ and be radiatively coupled (i.e., exchange CO line photons), which introduces a nonlocal contribution to the CO excitation.

Marti and Noerdlinger (1977) and Rybicki and Hummer (1978) worked out suitable generalizations of the basic Sobolev theory which take this radiative coupling into account. The vector formulation of the solution presented by Rybicki and Hummer makes it particularly useful for multidimensional geometries, and it was implemented in Bertout's (1979) code for solving the two-level atom line formation in axisymmetric envelopes. The role of radiative coupling was studied extensively with that code, and in most cases was found negligible for the source function computation. Radiative coupling becomes important only when the source function stays approximately constant over a large part of the envelope. In all cases where the line local excitation decreases with increasing radius (due, e.g., to dilution of the stellar radiation field or to decreasing density), we find that neglecting the radiative coupling generally results in a less than 10% effect on the emergent line flux from a spherically symmetric envelope. Because of the smaller solid angle sustained by the envelope, we expect the error to be even smaller in the biconical geometry considered here. Since computing the nonlocal coupling requires an integration over the whole envelope, the required computing time is an order of magnitude longer than in the case of a purely local source function (see Bertout 1979). Considering the many sources of uncertainties in our computations (CO/H_2 abundance ratio and CO to H_2 collision rates), we feel that the local approximation to the source function is sufficient for our purpose.

b) Line Profiles

Although we neglected nonlocal radiative interactions when determining CO excitation conditions, we did take them into account when computing emergent CO line profiles, the properties of which depend heavily on the detailed shape of constant velocity surfaces (see Rybicki and Hummer 1978). For

that purpose, the algorithm of Paper I was modified to handle nonmonotonical variations of the radial velocity along the lines of sight. This generalized algorithm was tested in the case of a spherical envelope with $\alpha = 0.5$ by comparing the total line flux, integrated over all lines of sight, with the flux given by an independent code that was thoroughly tested beforehand (Bertout 1984). The results presented in this paper were obtained by computing emergent CO line profiles along 1600 lines of sight that mapped the flow area on a square grid of 40 by 40 points.

III. RESULTS

As shown in Paper I, the spatial configurations of a radial biconical outflow relevant to the line formation problem can be divided into four categories, depending on the values of both θ_{max} (the flow opening angle) and i (the angle between the flow axis and the line of sight). Hence, general properties of the CO emission for a given flow model can all be deduced from results obtained in four configurations representative of each of these categories. Figures 1–4 present results for the CO ($J = 1 \rightarrow 0$) emission from a decelerated flow with $v(r) \propto 1/r$ (i.e., where $\alpha = 1$). The other parameters entering the computations have the following values: $\delta = 1$, $n_{H_2}(r_{min}) = 10^4$ cm^{-3}, $T_k = 10$ K, $k(r_{min}) = 2$, $\sigma = 5$, $\theta_{max} = 30°$ on Figures 1–3, and $\theta_{max} = 60°$ in Figure 4.

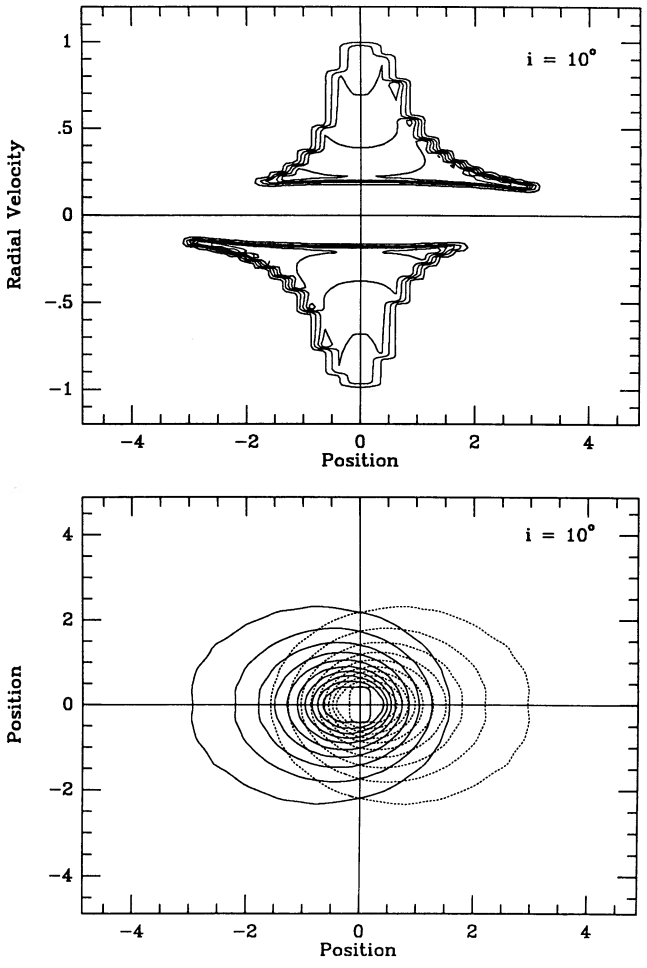

FIG. 1.—Results for a cone opening angle of 30° and an inclination angle $i = 10°$, illustrating case 1 (see text for values of other parameters). *Upper panel*: Spatial-velocity diagram showing contours of constant CO $J = 1 \rightarrow 0$ line temperature along the flow axis. Radial velocities are in units of v_{max} and position offsets in units of r_{min}. Lowest contour level, 0.1 K; second one, 1 K; step between other contours, 1 K. *Lower panel*: Contour map of integrated intensity in the blueshifted (*solid lines*) and redshifted (*dashed lines*) CO $J = 1 \rightarrow 0$ emission. Position offsets are in units of r_{min}. Lowest contour level 0.1 K × v_{max}, step between contours, 0.2 K × v_{max}.

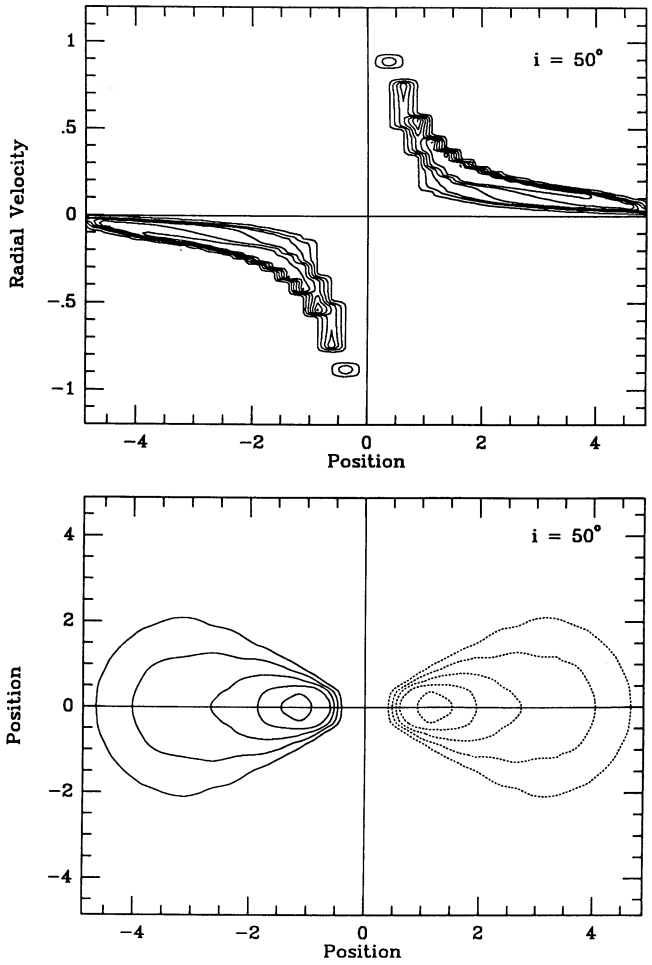

FIG. 2.—Same as Fig. 1 for an inclination angle $i = 50°$, illustrating case 2

In each of the four figures, the upper panel shows a position-velocity diagram where contours of equal line temperature $T_l = c^2/2kv^2[I_v - B_v(T_b)]$ are plotted as a function of radial velocity and position along the flow axis. The lower panel shows contours of integrated blueshifted (*solid lines*) and redshifted (*dashed lines*) intensities, which trace the spatial distribution of high-velocity emission. In both maps, radial velocities have been normalized to v_{max}, and position offsets are in units of r_{min}. Note that the velocity and position axes in spatial velocity diagrams have been switched with respect to Paper I, so that the x-axis now corresponds to position offset along the flow axis (as in integrated intensity maps). CO line emission from the static cloud itself has not been included in the spatial velocity diagrams, where it would appear as a narrow (~0.2 to 2 km s^{-1} FWHM) horizontal band centered on zero velocity. The following paragraphs describe the characteristics of the CO emission for each flow configuration.

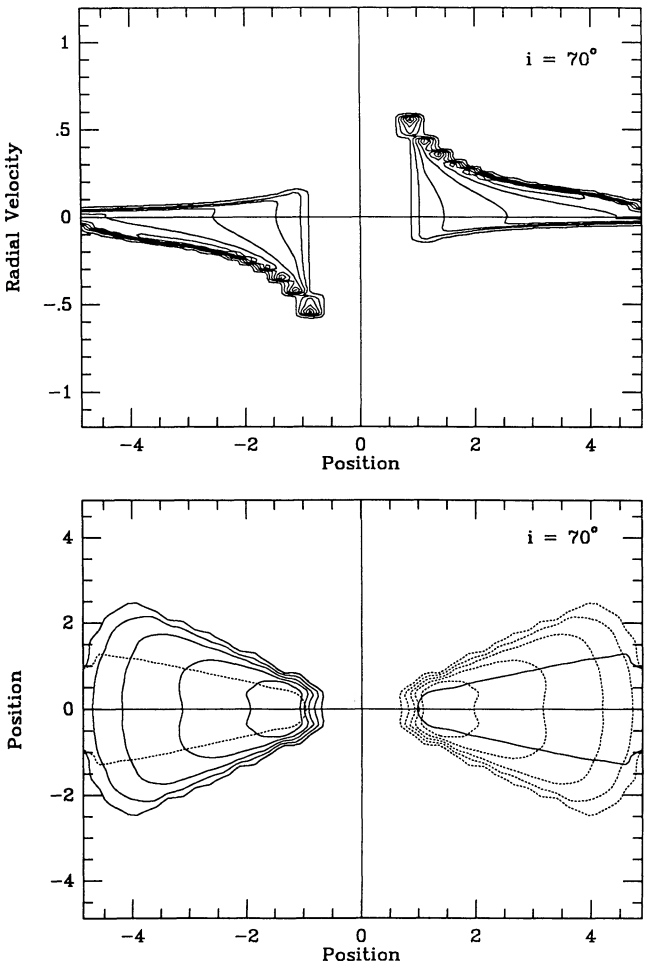

FIG. 3.—Same as Fig. 1 for an inclination angle $i = 70°$, illustrating case 3

a) Case 1 ($i < \theta_{max}$ and $i \leq 90° - \theta_{max}$)

This case is illustrated in Figure 1, where $i = 10°$ and $\theta_{max} = 30°$. Since $i < \theta_{max}$, central lines of sight intersect both cones of the flow, and resulting CO line profiles have a blueshifted and a redshifted component. The position-velocity diagram shows that the line wings are most prominent toward the central position. The maximum velocity in the profile gradually decreases as we look further away from the flow center, while the minimum velocity, which corresponds to emission from the slower outer layers of the flow, stays roughly constant with position. Since the flow is seen almost pole-on, the integrated intensity map shows circular and overlapping contours of blueshifted and redshifted emission.

b) Case 2 ($i \geq \theta_{max}$ and $i \leq 90° - \theta_{max}$)

This case occurs only if $\theta_{max} \leq 45°$ and is illustrated in Figure 2, where $i = 50°$ and $\theta_{max} = 30°$. The two cones now appear spatially separated. Each CO line profile probes only one high-velocity cone and is either blueshifted or redshifted, with a maximum radial velocity increasing progressively as one looks closer to the center of the flow. As a consequence and unlike in case 1, the position-velocity diagram shows a sharp discontinuity between blueshifted and redshifted profiles on each side of the star. Another difference with case 1 profiles is that low radial velocity emission is only found far out in the lobes. Profiles emitted close to the flow center only show high radial velocities and might, if actually observed, appear as a distinct high-velocity emission component displaced from the line core emitted by the static cloud. The integrated intensity map has a clear bipolar structure with a blue and a red lobe of high-velocity emission symmetrically displaced from the central source.

c) Case 3 ($i \geq \theta_{max}$ and $i > 90° - \theta_{max}$)

Illustrated in Figure 3, where $i = 70°$ and $\theta_{max} = 30°$, this case represents flows oriented almost in the plane of the sky, where the blueshifted cone (tilted toward us) has its rear side redshifted, while the redshifted cone (tilted away from us) has its front blueshifted. The position-velocity diagram differs from case 2 in that each CO line profile now extends from negative to positive velocities. The profiles are broadest next to the flow center at the position of highest maximum radial velocity. The integrated intensity map shows two separate lobes, each with superposed blue and red contours.

d) Case 4 ($i < \theta_{max}$ and $i > 90° - \theta_{max}$)

Whenever $\theta_{max} > 45°$, this case replaces case 2 as the intermediate configuration between cases 1 and 3. It is illustrated in Figure 4, where $i = 50°$ and $\theta_{max} = 60°$, and can be understood as a flow almost in the plane of the sky where, because of their

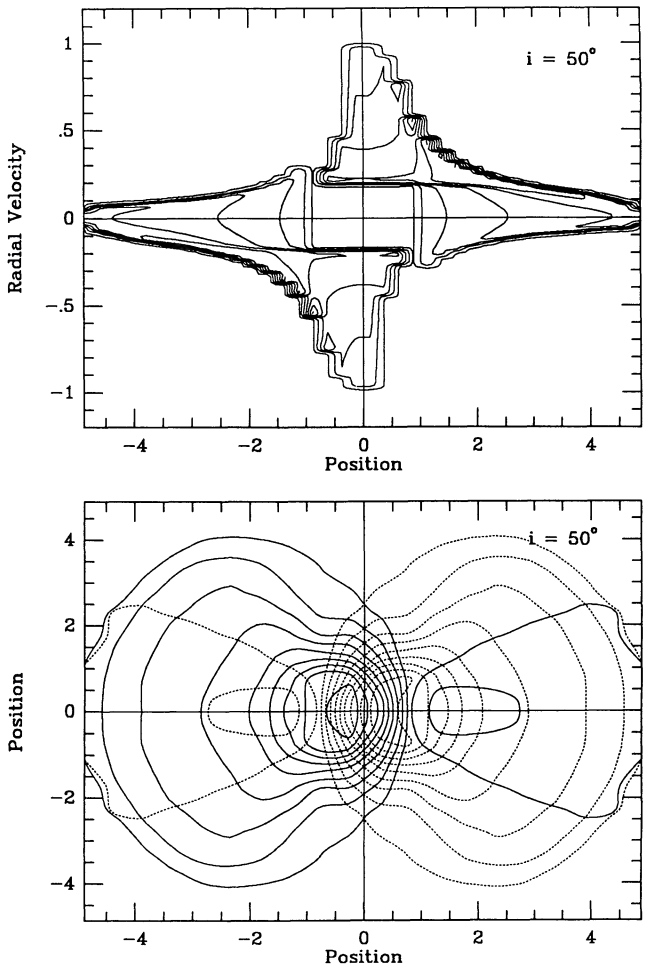

FIG. 4.—Same as Fig. 1 for a cone opening angle of 60° and an inclination angle $i = 50°$, illustrating case 4.

larger opening angle, the two cones still overlap along the central lines of sight. The spatial velocity map can be considered as the superposition of two maps: that of a case 1 flow (with $\theta_{max} = 30°$ and $i = 20°$) and that of a case 3 flow (with $\theta_{max} = 30°$ and $i = 80°$). The integrated intensity map also combines the characteristics of cases 1 and 3 shown in Figures 1 and 3, i.e., almost circular lobes overlapping toward the center of the flow and contamination of the blue and red lobes by red and blue emission further out.

IV. COMPARISON WITH OBSERVED FLOWS

a) Accelerated Flows versus Decelerated Flows

A comparison of the above results with Figures 2–5 of Paper I shows that integrated intensity maps of a decelerated flow are similar to those of accelerated and constant velocity flows in the same spatial configuration. Integrated intensity maps in fact only give information about the column density gradient in the flow and about the flow collimation and inclination from the plane of the sky. Position-velocity diagrams, on the other hand, differ widely from one flow model to the other, which makes them good indicators of the velocity field. Determining the velocity field of molecular flows would be extremely useful for putting constraints on possible mechanisms of flow ejection and collimation and for understanding the outflow's interaction with its surroundings. We will, therefore, attempt to determine which of the kinematic models investigated so far best reproduces the characteristics of observed flow in each configuration.

Possibly as a result of an observational selection effect, most high-velocity flows are observed almost pole-on (Case 1), where radial velocities and column densities are expected to be highest. Available position-velocity diagrams for flows that clearly appear to be in case 1 (T Tau, LkHα 198, AFGL 490, MWC 1080; R. Levreault, private communication) show a smooth decline in line-wing maximum velocity as one looks further from the flow center. This corresponds to the behavior of a decelerated case 1 model and contrasts with the behavior of an accelerated case 1 outflow, where emission from the faster outer layers of the flow produces narrow high-velocity wings at the periphery of the lobes, or of a constant velocity case 1 flow, which shows narrow high-velocity profiles almost independent of position (see Paper I).

Only a few well-studied outflows appear at higher inclination to the line of sight (i.e., in cases 2 and 3). These are L1551 IRS 5, Orion B, and R Mon for case 2 (e.g., Moriarty-Schieven and Snell 1988; Sanders and Willner 1985; Bachiller, Cernicharo, and Martin-Pintado 1987) and B335 and RNO 43 for case 3 (Moriarty-Schieven 1988; Cabrit, Goldsmith, and Snell 1988). In these well-resolved flows, the large-scale bipolar lobes appear highly collimated, with $\theta_{max} \leq 30°$, and (except in RNO 43, where the spatial resolution is inadequate for such a study), position-velocity diagrams show progressively higher radial velocities as one looks further from the center. These observations appear consistent with CO line computations for an accelerated bipolar flow, but not with a constant velocity or decelerated flow.

None of the simple kinematical models investigated in Paper I and here, therefore, seems able to simultaneously reproduce the observed properties of high-velocity flows in different configurations. There are several possible explanations to this situation.

1. When the flow is viewed almost pole-on (case 1), variations in velocity as a function of distance to the source affect position-velocity diagrams mostly through the flow's biconical geometry, because emission from the periphery of the lobes comes from points farther from the star. The shape of the diagram in this configuration is in fact much more sensitive to possible variations in velocity as a function of latitude. In contrast, position-velocity diagrams of flows that are more inclined with respect to the line of sight (cases 2 and 3) reflect mainly variations in velocity with distance from the flow source. A possible explanation for the observations is then that molecular flows are actually accelerated and that the apparent deceleration observed in pole-on flows is due to a decrease in flow velocity as one moves farther from the flow axis.

2. A variation on this model, recently suggested by Moriarty-Schieven and Snell (1988) for the L1551 IRS 5 flow, is that high-velocity CO emission arises from a curved hollow shell of molecular material swept up by a latitude-dependent stellar wind with velocity decreasing from the pole to the equatorial regions. Such a velocity field has been proposed to explain the forbidden line profile structure in T Tauri stars (Edwards *et al.* 1987) and was also suggested by the radial velocity progression of upper Balmer shell absorption features seen in the conical reflection nebula near the star R Mon (Jones and Herbig 1982). Because of the shell curvature, CO gas farther away from the star is impacted by wind ejected at higher latitudes and hence achieves a higher velocity. Moriarty-Schieven and Snell show that the combined variations in velocity magnitude and projection angle within the high-velocity shell result in an apparent acceleration if the flow is highly inclined to the line of sight. On the other hand, if the shell closes upon itself at some distance from the star (as would be expected if it results from the expansion of a "wind-bubble"; Weaver *et al.* 1977; Sakashita and Hanami 1986), the same flow seen pole-on should show lower radial velocities farther away from flow center.

3. Alternatively, we might be looking not at a homogeneous population of bipolar flows but rather at two groups with different opening angles: (*a*) a group of highly collimated flows ($\theta_{max} \leq 30°$) observed mainly in cases 2 or 3 (as predicted by our model), where high-velocity gas would be accelerated with distance from the source; (*b*) a group of almost isotropic outflows (with opening angles $\theta_{max} \geq 60°$) which would make up the bulk of known "pole-on" flows. All investigated velocity fields would then be compatible with their observed position-velocity diagrams, because gas projected at the periphery of the lobes would be moving in a direction almost perpendicular to the line of sight and always have a small radial velocity. However, higher resolution observations of pole-on flows are required in order to determine to which extent their poor apparent collimation is not due to a resolution effect.[2]

b) Hollow Lobes versus Filled Lobes

Another important question that has so far remained unsettled is whether the high-velocity CO gas is filling the flow lobes or is confined to their surface in a dense shell (Snell *et al.* 1984; Levreault 1985, 1988; Moriarty-Schieven and Snell 1988). Case 2 appears the best choice of flow configuration for investigating this issue, because the front and rear side of a hollow shell ought to give rise to two distinct velocity components of com-

[2] An example of this effect is the NGC 2071 outflow, which seemed to be in case 1 on a 90″ resolution map but was later shown to be in case 2 on maps made with 45″ and 23″ resolution (Snell 1987).

parable intensity toward the flow axis, instead of the single high-velocity component of a filled lobe (see e.g., Cabrit 1986). Only two case 2 flows have been observed at an adequate resolution for such a study: the L1551 IRS 5 outflow (Moriarty-Schieven *et al.* 1987; Uchida *et al.* 1987; Rainey *et al.* 1987; Moriarty-Schieven and Snell 1988; Fridlund *et al.* 1989) and the molecular flow around the young Herbig emission star R Mon (Bachiller, Cernicharo, and Martin-Pintado 1987). These two flows show remarkably similar properties: (1) their blueshifted high-velocity lobe coincides with an optical cometary nebula illuminated by the central object; (2) low-velocity CO emission (a few km s^{-1} from cloud velocity) is found mostly near the edges of the lobe, while high-velocity emission is concentrated toward the flow axis; and (3) high-velocity gas appears to accelerate linearly with distance along the flow axis.

These characteristics have been often interpreted in terms of hollow flow lobes. Low-velocity emission along the lobe edges then corresponds to gas that moves almost perpendicular to the line of sight, while high-velocity emission along the axis traces the front side of the shell in the blue lobe (and the rear side of the shell in the red lobe). However, the lower velocity component expected from the projection of the other side of the shell is not observed in either of the two flows. An explanation commonly invoked for the L1551 IRS 5 outflow is that the second velocity component is hidden within low-velocity static ambient cloud emission, i.e., that the inclination angle i is very close to $90° - \theta_{max}$ (e.g., Moriarty-Schieven and Snell 1988; Fridlund *et al.* 1989). But this explanation must be excluded for the R Mon flow because *no static emission* is detected toward the flow axis (as if most ambient material had been pushed aside or accelerated by the flow).

We therefore conclude that the lobes of the R Mon flow must be filled. The distinct spatial distribution of low- and high-velocity CO gas can then be explained if high-velocity CO emission comes from rapidly moving molecular gas accelerated along the flow axis, while low-velocity emission at the edges of the lobes is actually tracing a slower molecular envelope at the flow boundaries. Note that this latitude-dependent velocity law is similar to the one invoked in the previous section to explain apparent variations in flow velocity field with view angle. The absence of detectable low-velocity CO emission toward the R Mon flow axis further requires that the slowly moving flow envelope have a low opacity in order to be seen only toward the cone edges, where its column density and total optical depth are maximum.

A similar filled-lobe model was already suggested by Levreault (1985) based on CO $J = 2 \rightarrow 1$ observations of L1551 IRS 5. In this line, limb brightening of the low-velocity emission is much less apparent, which implies that low-velocity material is actually present toward the flow axis. Latitude-dependent velocity fields thus appear promising to explain both the apparent variation in flow's velocity field with viewing angle and the particular emission properties of two bipolar flows observed at high resolution. This model will be investigated quantitatively in a forthcoming paper.

V. OBSERVATIONAL UNCERTAINTIES IN FLOW PARAMETERS

Since the discovery of bipolar molecular outflows a decade ago (Zuckerman, Kuiper, and Rodriguez-Kuiper 1976; Kwan and Scoville 1976; Snell, Loren, and Plambeck 1980), a variety of procedures have been developed to derive the flow's global properties (e.g., its mass and momentum) from the high-velocity CO emission. One goal is to obtain the rates at which momentum and kinetic energy are transferred to the flow. This approach may help to constrain possible mass-loss mechanism in young stellar objects. However, it involves several sources of error (Lada 1985; Levreault 1988): (1) optical depth and excitation conditions of the CO transitions, (2) amount of outflowing gas that is projected at cloud velocity, (3) flow's velocity field, and (4) flow's inclination to the line of sight (that affects both the radial velocities and the apparent lobe sizes). Whether useful estimates of the flow parameters can still be obtained with simplifying assumptions about geometry and velocity field remains an issue. While an answer may depend on the type of flow that is considered, investigating this problem in detail for a simple flow model helps identify and quantify the sources of error present in the derivation.

In Paper I, we found that the simplest possible method, when applied to our synthetic CO profiles, did not provide accurate estimates of the true parameters of our models. In this paper, we extend our study to seven procedures currently used by various investigators to derive molecular flow properties. We applied all procedures to the same sets of synthetic ^{12}CO and ^{13}CO ($J = 1 \rightarrow 0$) profiles, computed for a series of decelerated, constant, and accelerated flow models ($\alpha = 1, 0, -1$) that spanned a ^{12}CO optical depth range of 1–6. ^{13}CO excitation was computed assuming an isotopic $^{12}CO/^{13}CO$ ratio of 89. Assumptions used in the various methods are summarized below, and their accuracy is discussed.

a) Mass Determination

The column density N_{obs} of high-velocity H_2 molecules along a particular line of sight can be estimated in two ways.

1. It can first be evaluated from the integrated intensity in the high-velocity wings of the ^{12}CO ($J = 1 \rightarrow 0$) line by assuming that the line is optically thin and thermalized at the kinetic temperature T_k, using

$$N_{obs} = \left(\frac{H_2}{^{12}CO}\right) \frac{3h}{8\pi^3\mu^2} \frac{1}{\Omega(T_k)} \int T_l{}^{12}(v)dv \,, \qquad (3)$$

where $\Omega(T_k) = x_0(T_k)(1 - e^{-h\nu/kT_k})[J_\nu(T_k) - J_\nu(T_b)]$, x_0 is the fraction of molecules in the $J = 0$ level ($\sim kT_{ex}/h\nu$), $J_\nu(T) = h\nu/k(e^{h\nu/kT} - 1)^{-1}$, and μ is the dipole moment of the CO molecule.

2. In flows where a ^{13}CO profile is available (generally only at the position of peak integrated ^{12}CO intensity), the ^{12}CO to ^{13}CO intensity ratio in the line wings ($\sim$10–20; Levreault 1988) is significantly lower than the terrestrial ^{12}CO to ^{13}CO isotopic ratio of 89, which indicates that high-velocity ^{12}CO emission is saturated. Since ^{13}CO high-velocity emission is probably optically thin anyway, opacity-corrected H_2 column densities can be calculated at all positions from the observed ^{12}CO emission by assuming that the $^{13}CO/^{12}CO$ integrated intensity ratio is independent of position in the flow.[3]

$$N_{obs} = \left(\frac{H_2}{^{13}CO}\right) \frac{3h}{8\pi^3\mu^2} \frac{1}{\Omega(T_k)} \left[\frac{\int_{peak} T_l{}^{13}(v)dv}{\int_{peak} T_l{}^{12}(v)dv}\right] \int T_l{}^{12}(v)dv \,. \qquad (4)$$

Once H_2 column densities have been obtained, the total H_2 mass in the flow can also be evaluated in two ways: (*i*) by assuming that the central line of sight is representative of the

[3] N_{obs} then depends only on the $[H_2/^{13}CO]$ abundance ratio, which is the quantity directly inferred from molecular cloud observations.

flow region, i.e.,

$$M_{\rm obs} = N_{\rm obs}(\text{center}) \times S_{\rm obs} \times m_{\rm H_2} , \quad (5)$$

where $S_{\rm obs}$ is the observed projected area of the flow; or (*ii*) by summing up the column densities over all observed positions if the flow has been sufficiently well sampled. We have then

$$M_{\rm obs} = \sum (N_{\rm obs}\, \delta S) \times m_{\rm H_2} . \quad (6)$$

Apart from additional refinements to be discussed later in this section, all procedures used so far to estimate flow mass correspond to one of the four possible combinations of the above assumptions. The errors introduced by the four procedures in determining total flow mass M_c are displayed in the upper panels of Figures 5–7 as a function of the view angle i for a decelerated, accelerated, and constant velocity flow model with $\tau \sim 6$. The error is measured in orders of magnitude by $\log (M_{\rm obs}/M_c)$. Each symbol in the plot corresponds to a different procedure, as summarized in Table 1. The true value of the flow mass was calculated analytically from

$$M_c = \omega f(\sigma) n_{\rm H_2}(r_{\rm min}) {r_{\rm min}}^3 m_{\rm H_2} , \quad (7)$$

where $\omega = 4\pi(1 - \cos \theta_{\rm max})$, $f(\sigma) = (\sigma^{\alpha+1} - 1)/(\alpha + 1)$ if $\alpha \neq -1$, $f(\sigma) = \ln(\sigma)$ if $\alpha = -1$, and the other parameters were defined in § II.

We find that the most accurate mass estimates are obtained for the procedure shown as a solid square in Figures 5–7 (e.g., Snell *et al.* 1984), which takes into account both ^{12}CO opacity (eq. [4]) and variations in column density over the flow area (eq. [6]). The mass estimate tends to be slightly too high in constant velocity and accelerated flows but tends to be slightly too small in decelerated flows. This result is at first surprising: one would intuitively expect the derived mass to be always too

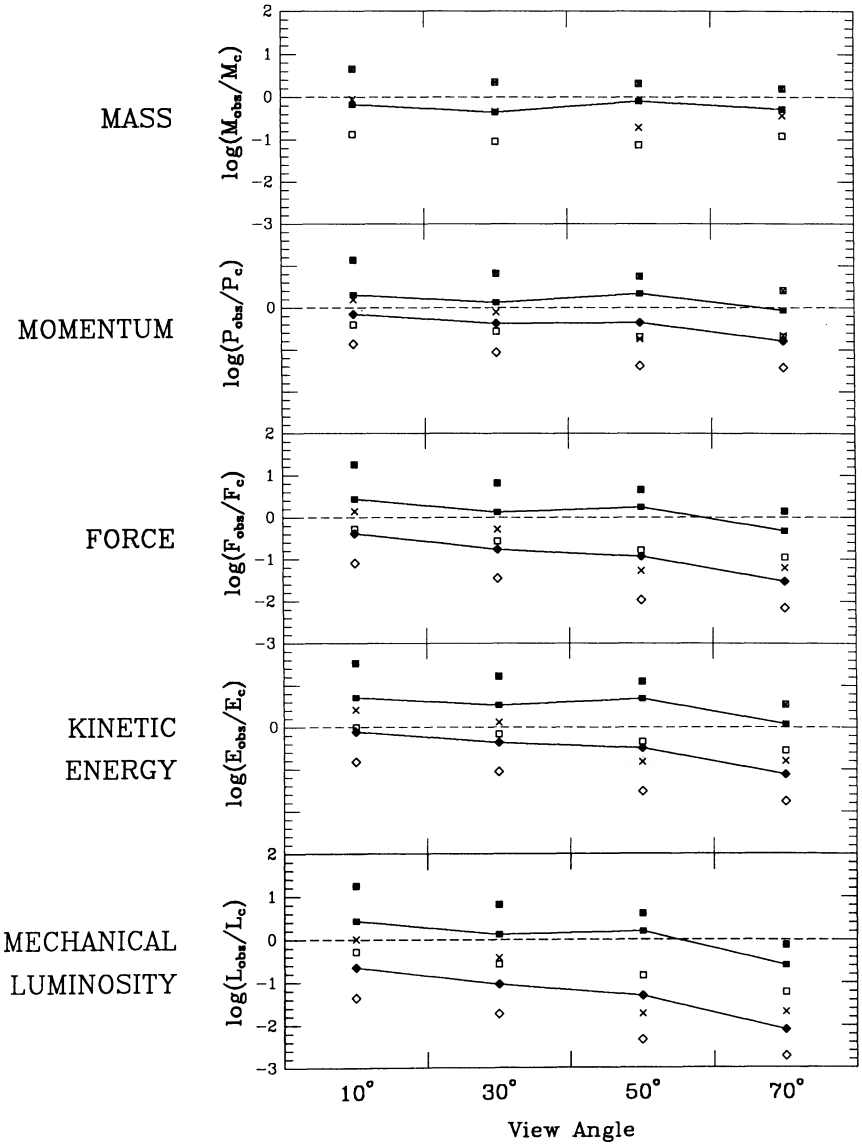

FIG. 5.—Errors on flow parameters derived from CO line profiles for an optically thick decelerated flow model with $v(r) \propto 1/r$ ($\alpha = 1$) seen at various view angles (see text for values of other parameters). The error on a given quantity Q is measured by $\log (Q_{\rm obs}/Q_c)$, where $Q_{\rm obs}$ is the value derived from the CO profiles and Q_c the correct value. Each symbol denotes a different procedure, as summarized in Table 1. Filled symbols are procedures that both use the best mass estimate, but assume either that all material is moving at the maximum observed radial velocity (*solid square*) or that material is flowing along the line of sight (*solid diamond*).

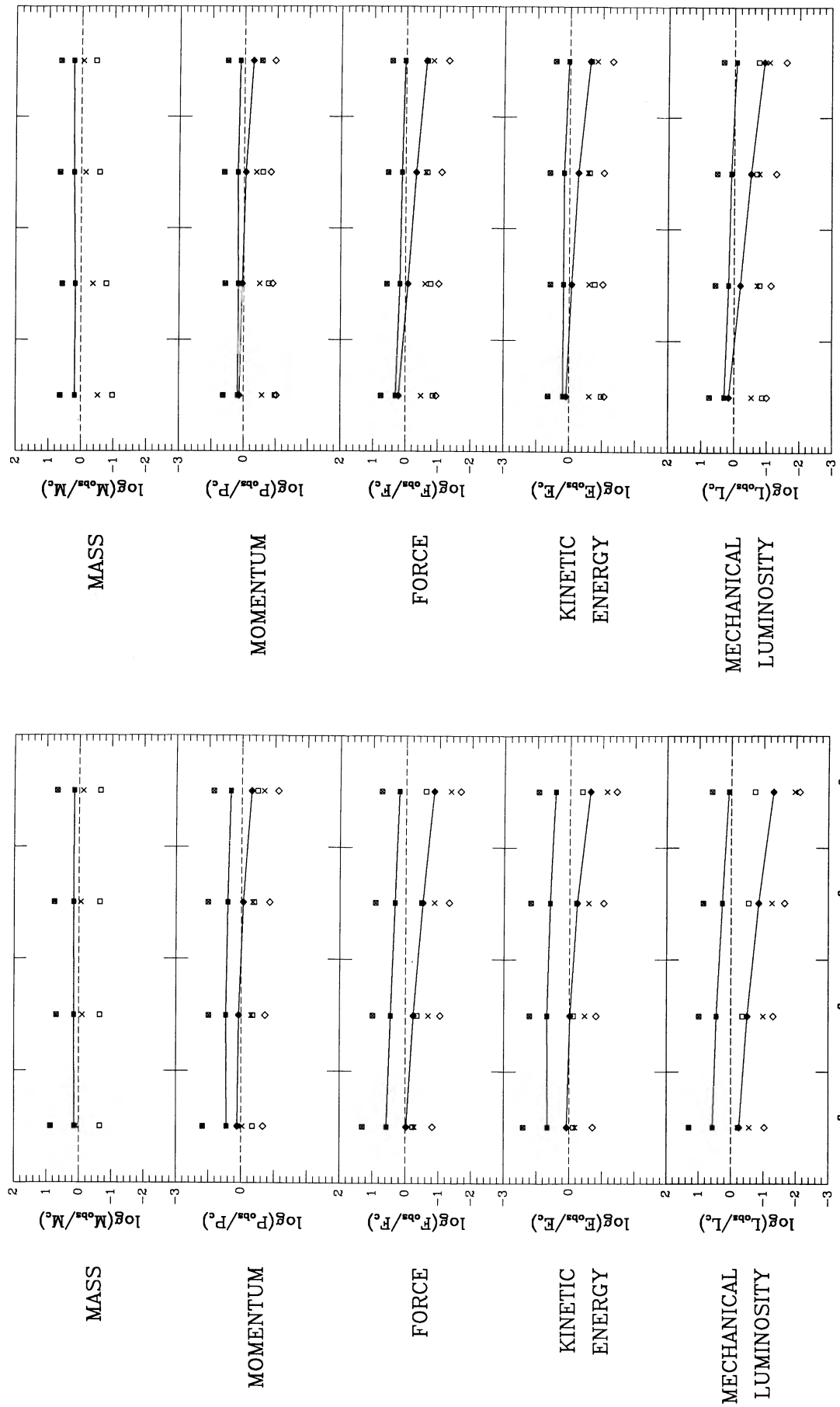

FIG. 6.—Same as Fig. 5 for an accelerated model with $v(r) \propto r$ ($\alpha = -1$)

FIG. 7.—Same as Fig. 5 for a constant velocity model ($\alpha = 0$)

TABLE 1

PROCEDURES FOR DERIVING FLOW PARAMETERS FROM CO DATA

SYMBOL IN FIGS. 5–7	FLOW MASS		FLOW VELOCITY	REFERENCES
	Corrected for ^{12}CO Opacity	Summed on All Positions	Maximum Velocity (else, intensity-weighted)	
Crossed square	Yes	No	Yes	1
Solid square	Yes	Yes	Yes	2
Solid diamond	Yes	Yes	No	3
Open square	No	Yes	Yes	4
Open diamond	No	Yes	No	5
Cross	No	No	No	6

REFERENCES.—(1) Bally and Lada 1983; (2) Lada 1985; (3) Margulis and Lada 1985; (4) Edwards and Snell 1982; (5) Edwards and Snell 1984; (6) Calvet, Cantó, and Rodriguez 1983.

high in optically thick flows, because the ^{13}CO/^{12}CO intensity ratio is measured at the position of peak ^{12}CO integrated intensity, where the optical depth should be larger than its actual mean value in the flow. But a detailed study of our complete set of synthetic profiles for the decelerated flow model shows that the ^{13}CO/^{12}CO ratio in fact peaks farther out in the flow, where it can be up to 5 times larger than at the ^{12}CO peak. This is probably because ^{13}CO integrated intensity reflects the true column density on the line of sight, while ^{12}CO integrated intensity reflects the velocity width of the profile when ^{12}CO is optically thick. If the flow is decelerated, the velocity width can decrease more steeply outward than the column density, and the ^{13}CO/^{12}CO integrated intensity ratio will increase. This interpretation is supported by the reverse tendency observed in accelerated flow models, where the integrated intensity ratio is maximum at a position closer to the center than that of the ^{12}CO peak. The ^{13}CO/^{12}CO ratio that is used is then larger than its mean value in the flow.

The procedure that sums up high-velocity ^{12}CO emission at all positions (eq. [6]) without attempting to correct it for opacity (eq. [3]) always gives a lower limit to the flow mass (e.g., Edwards and Snell 1984). The accuracy of this method, shown as an open square in Figures 5–7, is primarily determined by the optical depth in the flow. The resulting estimate is fairly good in an optically thin flow but is about an order of magnitude too small when $\tau \geq 4$.

In contrast, the method that corrects for ^{12}CO opacity (eq. [4]) but uses only a central line of sight (eq. [5]) always gives an upper limit to the mass (e.g., Bally and Lada 1983). The error in mass for this procedure, shown as a crossed box in Figures 5–7, is strongly dependent on the flow configuration. It increases from a factor 2 to 5 as the view angle i decreases from 70° to 10°.

By using only a central column density (eq. [5]) uncorrected for ^{12}CO opacity (eq. [3]) (e.g., Calvet, Cantó, and Rodriguez 1983), one combines the uncertainties present in the last two methods. As a result, the magnitude of the error depends both on the view angle and on the opacity in the flow. The derived mass (cross in Figs. 5–7) will be either too small (in most cases) due to ^{12}CO optical depth or too large if $\tau \leq 1$ and $i \leq 40°$. Similar results were found in Paper I for accelerated and constant velocity flows. Since the effect of this procedure is so hard to predict, it should not be used to derive constraints on the flow parameters.

The above analysis does not include recent attempts (e.g., Snell *et al.* 1984; Levreault 1985; Margulis and Lada 1985) to determine the CO excitation temperature T_{ex} from ^{13}CO and ^{12}CO ($J = 2 \rightarrow 1$) to ($J = 1 \rightarrow 0$) line ratios instead of assuming thermalization in equation (3). Estimated values of T_{ex} typically range from 8 to 30 K. However, these measurements are still uncertain because ^{12}CO and ^{13}CO may not have identical excitation conditions if the mean H_2 densities in the flows are less than 10^4 cm^{-3}. The presence along the line-of-sight of regions with differing optical depth or temperature may also seriously affect the line ratios (Cantó, Rodriguez, and Anglada 1987; Levreault 1988). As far as the mass estimate is concerned, the choice of a given value of T_{ex} does not appear critical, since the change in $\Omega(T)$ is small (less than a factor of 2 in the 8–30 K temperature range) with respect to all other uncertainties entering the derivation. And Figures 5–7 show that accurate masses can indeed be found by assuming that $T_{ex} = T_k$.

More difficult when dealing with actual CO observations is to evaluate the amount of high-velocity emission within the ambient cloud line core. While most observers prefer to exclude completely this velocity range from their computations in order to get lower limits to the integrated intensity of high-velocity gas, some authors (e.g., Bally and Lada 1983; Lada 1985; Margulis and Lada 1985) assume that the intensity of high-velocity gas emission is constant over the line core and equal to the average of the line temperature in the wings immediately outside this range. From the spatial velocity maps in Figures 1–4, it appears that this correction overestimates the flow mass in cases 1 or 2 by at least a factor of 2 if there is no overlap between line core and high-velocity emission. Conversely, not correcting for hidden low radial velocity material in a case 3 or case 4 flow might underestimate mass by a similar factor if the high-velocity gas homogeneously fills the observed lobes. To avoid overestimating flow mass, one should first determine which configuration applies. Given our poor knowledge of the actual geometry of most observed flows and the rarity of case 3 and case 4 flows, it seems quite reasonable at this point to ignore all emission within the line core.

In summary, we find that the true flow mass can be determined within 50% accuracy by summing up the contributions of all observed positions in the flow and then applying a global opacity correction to ^{12}CO column densities. Another possible approach consists in bracketing the actual value of the flow mass between the optically thin value (lower limit) and the opacity-corrected column density at the ^{12}CO peak times the flow area (upper limit). These two values typically differ by a factor of 30 in our models. We find that it is best not to attempt to correct for high-velocity material emitting within the

ambient line core, although one might then underestimate the flow mass by a factor ~ 2 if the flow has its axis highly inclined to the line of sight or is poorly collimated (cases 3 or 4).

b) Kinematic Parameters

Once column densities and flow mass have been determined, the total momentum P_{obs} and kinetic energy E_{obs} in the flow can be estimated in two ways:

1. One can assume that material in the flow is moving at a space velocity similar to the maximum observed radial velocity V_{obs} (e.g., Bally and Lada 1983), i.e.,

$$P_{obs} = M_{obs} \times V_{obs}$$
$$E_{obs} = \tfrac{1}{2} M_{obs} \times {V_{obs}}^2 . \quad (8)$$

2. With good signal-to-noise ratio observations, one can use the information contained in each independent velocity channel and assume that material in the flow is moving at a space velocity equal to the radial velocity at which it is detected, as if the gas was flowing along the line of sight (e.g., Margulis and Lada 1985), i.e.,

$$P_{obs} = \sum \left[\int m_{obs}(v) v \, dv \right] \delta S$$
$$E_{obs} = \tfrac{1}{2} \sum \left[\int m_{obs}(v) v^2 \, dv \right] \delta S , \quad (9)$$

where

$$m_{obs}(v) = M_{obs} \times T_l^{12}(v) \left\{ \sum \left[\int T_l^{12}(v) dv \right] \delta S \right\}^{-1} .$$

Note that the sum over all observed positions is restricted to a single term with $\delta S = S_{obs}$ if only a central line of sight is used (cf. eq. [5]).

Out of the eight possible combinations of the above assumptions with the four methods of mass determination presented in the previous section, only six have actually been used in practice and are summarized in Table 1. Resulting errors in determining the models' momentum and energy are plotted in the second and fourth panels of Figures 5–7. Symbols used in the first panel remain unchanged if the kinematic parameters were derived from flow mass using the maximum observed velocity (eq. [8]), but are rotated by 90° if only radial velocities were used (eq. [9]). The correct values for the flow's momentum P_c and kinetic energy E_c were computed from

$$P_c = \omega(\sigma - 1) v(r_{min}) n_{H_2}(r_{min}) {r_{min}}^3 m_{H_2}$$
and
$$E_c = \omega g(\sigma) \tfrac{1}{2} v(r_{min})^2 n_{H_2}(r_{min}) {r_{min}}^3 m_{H_2} , \quad (10)$$

where $g(\sigma) = (\sigma^{1-\alpha} - 1)/(1 - \alpha)$ if $\alpha \neq 1$ and $g(\sigma) = \ln(\sigma)$ if $\alpha = 1$.

In order to distinguish uncertainties entering the derivation of kinematic parameters from those affecting the mass determination, we will concentrate in the following paragraphs on results obtained with the two methods that most accurately determine flow mass, in conjunction with either equation (8) or equation (9).

Only taking into account the line-of-sight component of velocity (eq. [9]) always underestimates the true velocity of the emitting material. The error so introduced (*solid diamonds* in Figs 5–7) is due to projection effects and increases rapidly with the view angle i. The estimated flow momentum and kinetic energy are quite accurate at $i = 10°$, but they become about one order of magnitude too small at $i = 70°$.

On the other hand, adopting the maximum observed velocity tends to overestimate the mean velocity in the flow if an intrinsic velocity gradient is present, although this trend is weakened by projection effects. As a result, estimated momentum and energy (*solid squares* in Figs. 5–7) are always too large until $i = 70°$, where they approach their true values or may even be slightly smaller.

Actual values of the flow kinematic parameters thus almost always fall between estimates given by these two procedures. At small i, they are very close to the value obtained using line-of-sight velocities, while at large i the maximum observed velocity gives better estimates. Although neither of these procedures is particularly accurate, the use of both allows us to determine the flow's momentum within a factor ~ 5 and the flow's kinetic energy within one order of magnitude, provided mass is computed accurately.

c) Dynamic Parameters

One empirical procedure (e.g., Bally and Lada 1983; Snell *et al.* 1984) for estimating the input rate of a given flow parameter consists in dividing the total amount present in the flow by a characteristic flow time scale T_{obs} defined as the time needed to cross a characteristic flow dimension $\langle R \rangle$ (usually the maximum projected radius of the flow, R_{obs}) at a velocity $\langle V \rangle = P_{obs}/M_{obs}$. The force F_{obs} and mechanical luminosity L_{obs} in the flow are then determined by

$$F_{obs} = P_{obs}/T_{obs}$$
and
$$L_{obs} = E_{obs}/T_{obs} , \quad (11)$$

where $T_{obs} = \langle V \rangle / \langle R \rangle$.

Another approach (e.g., Edwards and Snell 1984; Calvet, Cantó, and Rodriguez 1983) consists in estimating the mean rate of momentum and energy transfer along the flow by summing up the contributions of elementary momentum fluxes $[\propto T_l(v) v^2 \, dv]$ and kinetic energy fluxes $[\propto \tfrac{1}{2} T_l(v) v^3 \, dv]$ at all positions in the flow, and by dividing them by the observed length of the lobe R_{obs}:

$$F_{obs} = 1/R_{obs} \sum \left[\int m_{obs}(v) v^2 \, dv \right] \delta S$$
$$L_{obs} = 1/R_{obs} \sum \left[\tfrac{1}{2} m_{obs}(v) v^3 \, dv \right] \delta S . \quad (12)$$

The actual momentum and kinetic energy input rates that are needed to bring outflowing material to its maximum velocity are[4]

$$F_c = \omega v_{max} v(r_{min}) n_{H_2}(r_{min}) {r_{min}}^2 m_{H_2}$$
and
$$L_c = \omega \tfrac{1}{2} {v_{max}}^2 v(r_{min}) n_{H_2}(r_{min}) {r_{min}}^2 m_{H_2} . \quad (13)$$

From equations (10) and (13), we derive the correct time scales for momentum and energy input:

$$T_c(P) = P_c/F_c = (r_{max} - r_{min})/v_{max}$$
and
$$T_c(E) = E_c/L_c = g(\sigma) r_{min}/v_{max} . \quad (14)$$

Note that the formula for $T_c(P)$ is a direct consequence of mass

[4] In Paper I, we considered only the momentum and energy input at the base of the flow ($r = r_{min}$), as would be appropriate if acceleration was due to external forces (e.g., pressure gradients in the surrounding medium). F_c and L_c are then smaller than in eq. (13) by a factor of σ^{α} and $\sigma^{2\alpha}$, respectively, and errors in F_{obs} and L_{obs} would be correspondingly higher.

conservation in the flow, while $T_c(E)$ depends on the velocity field in the flow and can be larger or smaller than $T_c(P)$. While the characteristic model input velocity is v_{max} for both time scales, the characteristic model transfer length is $(\sigma - 1)r_{min}$ (i.e., the true length of the flow lobe) for momentum, and $g(\sigma)r_{min}$ for energy. The accuracy of the various methods for estimating F_c and L_c then depends on errors in the characteristic transfer length and velocity, combined with previous errors in the derivation of P_{obs} and E_{obs}.

Most investigators adopt the observed length of the flow lobe, R_{obs}, as a characteristic dimension, although Snell *et al.* (1984) use half the distance between the blue and red centroids (usually $\sim R_{obs}/2$). The first choice seems more appropriate to estimate $T_c(P)$, while the second would be more appropriate for $T_c(E)$ if the flow is decelerated. However, in observed flows where the actual velocity field is unknown, using R_{obs} seems more realistic because it gives a true average of the momentum and energy flux along the flow axis. In particular, it would give the correct value of the momentum and energy transfer rates if they were constant along the flow, while the second choice would systematically overestimate them by a factor of 2.

The main difference between the various methods lies in the choice of the characteristic input velocity $\langle V \rangle$: if kinematic parameters are computed using the maximum observed velocity V_{obs} (eq. [8]), then $\langle V \rangle = V_{obs}$. But if only line-of-sight velocities are used to compute the flow parameters (eq. [12]), the characteristic velocities for momentum and energy transfer will be $F_{obs}R_{obs}/P_{obs}$ and $L_{obs}R_{obs}/E_{obs}$ (the former being always smaller than the latter), which are both smaller than V_{obs}.[5]

Since R_{obs} increases and $\langle V \rangle$ decreases as the flow is more inclined to the line of sight, estimated time scales become longer at higher view angles. However, the magnitude of the error is difficult to predict because R_{obs} also depends on the flow's opening angle (especially when the flow is seen pole-on) while $\langle V \rangle$ also depends on the velocity field. We find that both time scales are always underestimated at small view angles ($i \sim 10°$), but become overestimated at high view angles. Resulting errors in the dynamic parameters are plotted in the third and last panels of Figures 5–7 for the six methods studied in the previous section. The following paragraphs discuss errors for the two methods using the best mass estimates (*filled symbols*).

Since momentum and energy calculated from line-of-sight velocities were already lower limits to their true values, momentum and energy transfer rates obtained with the same assumption (eq. [12]; *solid diamonds* in Figs. 5–7) are always too small, by as much as a factor of 25 and 100, respectively, when $i = 70°$. At the same time, because kinematic parameters obtained with the maximum observed velocity V_{obs} were sufficiently overestimated, corresponding rates (eq. [11]; *solid squares* in Figs 5–7) remain too large as long as $i < 60°$. At higher inclinations, the derived rates come closer to their true values due to projection effects, and even become a factor of 2–5 too small in decelerated flows. However, if the flow is in the case 3 configuration (which is likely at such large view angles) and if θ_{max} can be independently estimated (e.g., from the apparent flow's opening angle on the integrated intensity map), it becomes possible to estimate the value of i and hence to correct V_{obs} for projection effects.

This procedure, which was recently applied by Cabrit, Goldsmith, and Snell (1988) to observed case 3 flows, is based on the fact that the maximum blueshifted and redshifted velocities observed at a given point along the flow axis correspond to the line-of-sight velocities of the front and rear sides of the high-velocity lobe. If the lobe is assumed to be a cone in a radial expansion from the star, the ratio $R \geq 1$ of these velocities is equal to $\cos(i - \theta_{max})/|\cos(i + \theta_{max})|$, and i can be derived from the ratio R using

$$\tan i = \frac{R+1}{R-1} \times \frac{1}{\tan \theta_{max}} .$$

One can then correct the observed maximum velocity V_{obs} for inclination by dividing it by $\cos(i - \theta_{max})$. If such a correction is applied to models with $i > 60°$, dynamical parameters obtained with V_{obs} remain upper limits even at large view angles.

Thus, the true dynamical parameters can also be bracketed between values obtained with these two procedures as long as V_{obs} is corrected for inclination at high view angles. Figures 5–7 show that the range of possible flow parameters between these two limits increases with view angle but remains less than a factor of 30 for F_c and less than a factor of 100 for L_c. Typical errors are of the order of 10 and 30, respectively.

V. SUMMARY

We extend here our earlier study of CO line formation in high-velocity bipolar flows to decelerated velocity fields. These results are used together with previous computations for accelerated and constant velocity fields to discuss observational constraints on the large-scale properties of bipolar flows. We find that the velocity field in observed flows seems to change with view angle: from decelerated in pole-on flows to accelerated in flows that are more inclined to the line of sight. We also discuss recent observations of the R Mon outflow, which suggest that the flow lobes are filled. The most promising model to explain these various aspects involves a bright high-velocity accelerated molecular jet surrounded by a low-opacity slower envelope. Such a latitude-dependent velocity field may naturally arise if high-velocity material along the flow edges is slowed down by friction with the surrounding medium, or if the underlying wind driving the flow is centrifugally ejected from a rotating accretion disk (Pudritz and Norman 1986). This flow pattern will be investigated in detail in a forthcoming paper.

Our model also allows us to estimate the accuracy of various methods currently used by observers to derive the parameters of bipolar flows from CO data. We find that flow mass can be determined within a factor of 2 by computing H_2 column densities at all positions in the flow (assuming optically thin ^{12}CO emission in LTE) and by applying a global opacity correction, estimated from the $^{13}CO/^{12}CO$ intensity ratio at the peak of ^{12}CO integrated intensity. We also confirm within the limits of our model the suggestion by Margulis and Lada (1985) that the kinematic and dynamic parameters of the flow can be bracketed between a lower limit obtained by considering only the line of sight component of the velocities and an upper limit obtained by assuming that the entire flow moves at the maximum observed velocity, although correcting these latter

[5] Snell *et al.* (1984) use yet another characteristic velocity equal to the mean intensity weighted line-of-sight velocity P_{obs}/M_{obs}, which is typically a factor of 2 smaller than $F_{obs}R_{obs}/P_{obs}$. However, this difference is compensated for by their choice of $R_{obs}/2$ as a characteristic dimension. Parameters obtained with this seventh method are therefore similar to those obtained using eq. (12) and are not plotted in Figs. 5–7.

values for inclination may be necessary at large view angles ($i > 70°$). Final uncertainties in model flow parameters are typically a factor of ~ 5 for P_c, 10 for F_c and E_c, and 30 for L_c, provided flow mass is carefully estimated using the procedure outlined above. Actual uncertainties for observed flows are probably twice as large because of uncertainties in the choice of the velocity ranges where high-velocity emission dominates over static cloud emission.

Finally, we find that flow masses estimated with different procedures can differ by a factor ~ 30 when applied to the same set of CO data. The resulting spread in estimated flow parameters then reaches two to three orders of magnitude. In view of this result, it becomes obvious that no clear understanding of the mass-loss mechanism will be gained from the study of bipolar flow parameters unless one looks at a homogeneous set of data, with flow masses that involve the same assumptions and H_2/CO abundance ratios.

REFERENCES

Bachiller, R., Cernicharo, J., and Martin-Pintado, J. 1987, *Pub. Astr. Inst. Czechoslovakian Acad. Sci.*, Vol. **4**, No. 65, p. 29.
Bally, J., and Lada, C. J. 1983, *Ap. J.*, **265**, 824.
Bertout, C. 1977, *Astr. Ap.*, **58**, 153.
———. 1979, *Astr. Ap.*, **80**, 138.
———. 1984, *Ap. J.*, **285**, 269.
Boss, A. P. 1987, *Ap. J.*, **316**, 721.
Cabrit, S. 1986, *Bull. AAS*, **18**, 1027.
Cabrit, S., and Bertout, C. 1986, *Ap. J.*, **307**, 313 (Paper I).
———. 1987, in *Protostars and Molecular Clouds*, ed. T. Montmerle and C. Bertout (Saclay: CEA/Doc), p. 42.
Cabrit, S., Goldsmith, P. F., and Snell, R. L. 1988, *Ap. J.*, **334**, 196.
Calvet, N., Cantó, J., and Rodríguez, L. F. 1983, *Ap. J.*, **268**, 739.
Cantó, J., Rodríguez, L. F., and Anglada, G. 1987, *Ap. J.*, **321**, 877.
Carroll, T. J., and Goldsmith, P. F. 1981, *Ap. J.*, **245**, 891.
Draine, B. T., and Roberge, W. G. 1984, *Ap. J.*, **282**, 491.
Edwards, S., and Snell, R. 1982, *Ap. J.*, **261**, 151.
———. 1984, *Ap. J.*, **281**, 237.
Edwards, S., Cabrit, S., Strom, S. E., Heyer, I., Strom, K. M., and Anderson, E. 1987, *Ap. J.*, **321**, 473.
Fridlund, C. V. M., Sandqvist, A., Nordh, H. L., and Olofsson, G. 1989, *Astr. Ap.*, **213**, 310.
Jones, B. F., and Herbig, G. H. 1982, *A.J.*, **87**, 1223.
Kwan, J., and Scoville, N. 1976, *Ap. J.*, **210**, L39.
Lada, C. J. 1985, *Ann. Rev. Astr. Ap.*, **23**, 267.
Lane, A. P., and Bally, J. 1986, *Ap. J.*, **310**, 820.
Leung, C. M. 1975, *Ap. J.*, **199**, 340.
Levreault, R. M. 1985, Ph.D. thesis, Department of Astronomy, University of Texas at Austin.
Levreault, R. M. 1988, *Ap. J. Suppl.*, **67**, 283.
Margulis, M. S., and Lada, C. J. 1985, *Ap. J.*, **299**, 925.
Martí, F., and Noerdlinger, P. D. 1977, *Ap. J.*, **215**, 247.
Moriarty-Schieven, G. H. 1988, Ph.D. thesis, Astronomy Department, University of Massachusetts, Amherst.
Moriarty-Schieven, G. H., Snell, R. L., Strom, S. E., Schloerb, F. P., Strom, K. M., and Grasdalen, G. L. 1987, *Ap. J.*, **319**, 742.
Pudritz, R. E. 1988, in *Galactic and Extragalactic Star Formation*, ed. R. E. Pudritz and M. Fich (Dordrecht: Kluwer), p. 135.
Pudritz, R. E., and Norman, C. A. 1986, *Ap. J.*, **301**, 571.
Rainey, R., White, G. J., Richardson, K. J., Griffin, M. J., Gronin, N. J., Monkiro, T. S., and Hilton, J. 1987, *Astr. Ap.*, **179**, 237.
Rybicki, G. B., and Hummer, D. G. 1978, *Ap. J.*, **219**, 654.
Sakashita, S., and Hanami, H. 1986, *Pub. Astr. Soc. Japan*, **38**, 879.
Sanders, D. B., and Willner, S. P. 1985, *Ap. J. (Letters)*, **293**, L39.
Snell, R. L. 1987, in *Star Forming Regions*, ed. M. Peimbert and J. Jugaku (Dordrecht: Reidel), p. 213.
Snell, R. L., Loren, R. B., and Plambeck, R. L. 1980, *Ap. J. (Letters)*, **239**, L17.
Snell, R. L., Scoville, N. Z., Sanders, D. B., and Erickson, N. R. 1984, *Ap. J.*, **284**, 176.
Sobolev, V. V. 1957, *Soviet. Astr.–AJ*, **1**, 678.
Storey, J. W. V., *et al.* 1989, *M.N.R.A.S.*, **237**, 1001.
Uchida, Y., Kaifu, N., Shibata, K., Hayashi, S. S., and Hasegava, T. 1987, in *Star Forming Regions*, ed. M. Peimbert and J. Jugaku (Dordrecht: Reidel), p. 287.
Weaver, R., McCray, R., Castor, J., Shapiro, P., and Moore, R. 1977, *Ap. J.*, **218**, 377.
Zuckerman, B., Kuiper, T. B. H., and Rodriquez-Kuiper, E. N. 1976, *Ap. J. (Letters)*, **209**, L137.

CLAUDE BERTOUT and SYLVIE CABRIT: Institut d'Astrophysique, 98 bis Bd. Arago, F-75014 Paris, France